AGU PUBLICATIONS

JGR

Journal of Geophysical Research: Solid Earth

RESEARCH ARTICLE
10.1002/2016JB012793

Key Points:
- Coignimbrite plumes act as an efficient mechanism of ash injection into the atmosphere
- Sensitivity analysis enables investigation of relationship between model inputs and plume height
- Initial flow mass flux controls both location of plume formation and maximum plume height

Supporting Information:
- Supporting Information S1

Correspondence to:
S. L. Engwell,
samantha@engwell.com

Citation:
Engwell, S. L., M. de' Michieli Vitturi, T. Esposti Ongaro, and A. Neri (2016), Insights into the formation and dynamics of coignimbrite plumes from one-dimensional models, *J. Geophys. Res. Solid Earth*, *121*, 4211–4231, doi:10.1002/2016JB012793.

Received 4 JAN 2016
Accepted 16 MAY 2016
Accepted article online 23 MAY 2016
Published online 22 JUN 2016

Insights into the formation and dynamics of coignimbrite plumes from one-dimensional models

S. L. Engwell[1,2], M. de' Michieli Vitturi[1], T. Esposti Ongaro[1], and A. Neri[1]

[1]Istituto Nazionale di Geofisica e Vulcanologia, Sezione di Pisa, Pisa, Italy, [2]Now at British Geological Survey, Edinburgh, UK

Abstract Coignimbrite plumes provide a common and effective mechanism by which large volumes of fine-grained ash are injected into the atmosphere. Nevertheless, controls on formation of these plumes as a function of eruptive conditions are still poorly constrained. Herein, two 1-D axysymmetric steady state models were coupled, the first describing the parent pyroclastic density current and the second describing plume rise. Global sensitivity analysis is applied to investigate controls on coignimbrite plume formation and describe coignimbrite source and the maximum plume height attained. For a range of initial mass flow rates between 10^8 and 10^{10} kg/s, modeled liftoff distance (the distance at which neutral buoyancy is attained), assuming radial supercritical flow, is controlled by the initial flow radius, gas mass fraction, flow thickness, and temperature. The predicted decrease in median grain size between flow initiation and plume liftoff is negligible. Calculated initial plume vertical velocities, assuming uniform liftoff velocity over the pyroclastic density current invasion area, are much greater (several tens of m/s) than those previously used in modeling coignimbrite plumes (1 m/s). Such velocities are inconsistent with the fine grain size of particles lofted into coignimbrite plumes, highlighting an unavailability of large clasts, possibly due to particle segregation within the flow, prior to plume formation. Source radius and initial vertical velocity have the largest effect on maximum plume height, closely followed by initial temperature. Modeled plume heights are between 25 and 47 km, comparable with Plinian eruption columns, highlighting the potential of such events for distributing fine-grained ash over significant areas.

1. Introduction

Coignimbrite plumes form in association with propagating pyroclastic density currents (PDCs) [*Sparks et al.*, 1997]. Such plumes can rise tens of kilometers into the atmosphere, dispersing ash over the entire continents. The fine-grained nature of the ash means that the risk posed by such events is significant, with potential implications for aviation and on deposition, infrastructure, and health [*Horwell et al.*, 2001]. Resultant coignimbrite deposits have consistent grain size characteristics, regardless of eruption type (chemistry and magnitude) or type of current (ignimbrite forming to block and ash flows) [*Engwell and Eychenne*, 2016]. This observation leads to a number of key questions: what controls the grain size of ash lofted into coignimbrite plumes, what are the conditions required for coignimbrite plume formation, and what controls the height to which these plumes rise in the atmosphere?

The mechanism of coignimbrite plume formation has been investigated both experimentally [*Carey and Sigurdsson*, 1988; *Huppert et al.*, 1986; *Sparks et al.*, 1993; *Woods and Caulfield*, 1992; *Andrews and Manga*, 2012] and numerically [*Woods and Wohletz*, 1991; *Woods and Kienle*, 1994; *Bursik and Woods*, 1996; *Calder et al.*, 1997; *Neri and Dobran*, 1994; *Herzog and Graf*, 2010]. Coignimbrite plumes form due to buoyancy reversal of PDCs. Coarse material is deposited as PDCs propagate, and fine material (<100 μm in diameter) becomes concentrated at the top of the current [*Valentine*, 1987; *Druitt*, 1998], (Figure 1). The turbulent nature of the current encourages entrainment of ambient air, which is heated by the particles, leading to thermal expansion. Consequently, the mixture of air and particles becomes less dense than the surrounding atmosphere and separates from the current. Observations [*Sparks et al.*, 1986], experimental studies [*Andrews and Manga*, 2012, 2011], and numerical simulations [*Esposti Ongaro et al.*, 2008, 2012] have shown that the location of this "liftoff" can be associated with current termination and may have an effect on current behavior downstream of lofting location. As the plume rises through the atmosphere, air continues to be entrained. For strong plumes, the plume rises and passes the level of neutral buoyancy due to inertia, reaching its maximum height, where the vertical velocity decreases to zero and falls back to the neutral buoyancy

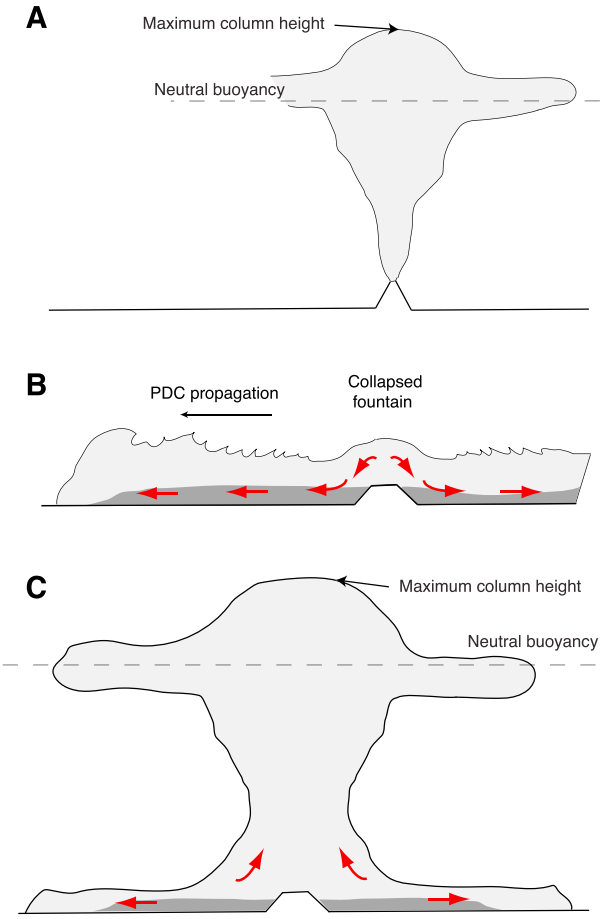

Figure 1. Schematic showing formation of coignimbrite plumes [after *Woods and Wohletz*, 1991]. (a) A typical Plinian plume showing plume rise from the eruptive vent and distinguishing maximum column height from neutral buoyancy height. (b) In the simulations, collapse of such a plume is assumed to result in the formation of pyroclastic density currents (PDCs) or ash flows which propagate radially from the collapsed fountain, entraining ambient air and sedimenting particles as they propagate. (c) The coignimbrite plume forms once the upper portion of the current reaches a density equal to the ambient and is assumed to loft from the whole flow to this distance. Note that this distance may be shorter than the actual PDC runout. Maximum plume height and neutral buoyancy levels are characterized in the same way as for Plinian examples.

where it spreads laterally (Figure 1). Proximal deposition of ash is predominantly as aggregates, with resulting deposits containing abundant accretionary lapilli [*Eychenne et al.*, 2012]. Depositional processes in the more distal plume are poorly understood [*Engwell and Eychenne*, 2016].

As a result of formation in association with PDC propagation, rather than directly from an eruptive vent, source conditions of coignimbrite plumes vary considerably compared with those of Plinian plumes. Multiple discrete coignimbrite plumes that merge at height often form in association with the interaction of channel-confined PDCs with topography, for example, during the 1995–2010 activity of Soufrière Hills, Montserrat [*Bonadonna et al.*, 2002; *Calder et al.*, 1997; *Cole et al.*, 1998]. When only a single plume is inferred, the initial radius is much larger. Observations and photographs of the Mount St. Helens 18 May 1980 coignimbrite plume show that the plume lofted from an area of ≈600 km^2 (the area invaded by the PDC), whereas isopachs of the coignimbrite deposit from the 29 May 1991 block-and-ash flow at Fugendake, Unzen, show an elongate source indicating plume rise from the entire length of the flow runout [*Watanabe et al.*, 1999].

The initial vertical velocity of coignimbrite plumes inferred from observations is much lower [*Woods and Wohletz*, 1991; *Woods and Kienle*, 1994; *Calder et al.*, 1997] than for Plinian plumes (on the order of hundreds of m/s). *Calder et al.* [1997] used photographs to infer initial vertical velocities of 1–2 m/s for the coignimbrite plumes that rose from the 18 August pumice flows, Mount St. Helens, and such a value is commonly used in the application of numerical models when modeling coignimbrite plume rise [*Woods and Wohletz*, 1991]. The initial vertical velocity has a direct consequence on the rising plume's ability to carry particles, with Plinian plumes able to carry large (tens of centimeters) particles high into the atmosphere, while the inferred grain size carried by coignimbrite plumes is much smaller [*Engwell and Eychenne*, 2016]. Coignimbrite plumes may also inherit horizontal velocity characteristics from the parent PDC, for example, the 18 May Mount St. Helens coignimbrite plume was bent to the north, the main propagation of PDC direction, with implications for plume rise and intrusion into the atmosphere [*Eychenne et al.*, 2015].

Despite these differences in source conditions, coignimbrite plumes are able to reach great altitudes, with the Mount St. Helens 18 May 1980 and 15 June 1991 Pinatubo coignimbrite plumes both reaching heights of 30 km [*Sparks et al.*, 1986; *Holasek et al.*, 1996]. Even small-magnitude events are able to form coignimbrite plumes which rise many kilometers in the atmosphere; during dome collapse at Mount Redoubt in 1990 two coignimbrite plumes were formed which both lofted to heights of 12 km [*Woods and Kienle*, 1994].

Coignimbrite plume interaction with the atmosphere is similar to that of for vent-derived plumes, whereby plumes with low mass flow rates rise can be strongly affected by the wind [*Watanabe et al.*, 1999; *Miyabuchi*, 1999], while observations (for example, from the 18 May Mount St. Helens and the Pinatubo 1991 eruptions) show that coignimbrite plumes with high mass flow rates are less sensitive to wind. In the Pinatubo 1991 and Mount St. Helens 18 May 1980 examples, there is a significant difference between maximum plume height and the height at which the plume intrudes laterally into the atmosphere (neutral buoyancy level, Figure 1) [*Sparks et al.*, 1986]. In the Mount St. Helens example, this "overshoot" was on the order of about 10 km [*Sparks et al.*, 1986; *Eychenne et al.*, 2015].

Application of numerical plume models is key for constraining source conditions for tephra transport models, and proper consideration of the differences between Plinian and coignimbrite plumes is essential. Two numerical models have been proposed to model the rise of coignimbrite plumes. Coignimbrite plumes have been modeled as both steady state columns [*Woods and Wohletz*, 1991; *Calder et al.*, 1997], by adapting the model of *Woods* [1988], and as buoyant thermals [*Woods and Kienle*, 1994]. In the steady state example of *Woods and Wohletz* [1991], the upper portions of the pyroclastic flows become buoyant through the entrainment, heating, and subsequent expansion of ambient air. Application of steady state models requires three main assumptions: first that the plume originates from a finite area (corresponding to the area inundated by the PDC); initial velocity is small; and finally, and most importantly, that the pyroclastic flow acts as a continuous source of ash and hot gas over timescales longer than the ascent time of the coignimbrite plume. In application of the model, *Woods and Wohletz* [1991] apply a constant radial entrainment coefficient with height; however, *Calder et al.* [1997] investigate more complex entrainment relationships to account for the large source radius relative to column height near the source, which results in inefficient entrainment near the base of the plume, becoming more efficient with height as the plume radius reduces (Figure 1). Comparison of model results using these different entrainment assumptions shows little variation in plume height [*Sparks et al.*, 1997]. The model allows prediction of column height, which for a given total eruptive mass flux at vent is much lower for coignimbrite columns than Plinian examples. This is because only a portion of the erupted mass flux lofts to form the coignimbrite plume, and due to entrainment and particle sedimentation during current propagation, the lofted mixture has a much greater percentage of ambient air, reaching 30–60% of the total mass compared to 1–5 wt % of gas (mostly water vapor) for Plinian columns. Moreover, entrainment during current propagation leads to much lower initial plume temperatures than for Plinian plumes.

Woods and Kienle [1994] apply a simple thermodynamic model, simulating plume rise as a buoyant thermal, to reproduce the coignimbrite plume rise at Redoubt volcano in April 1991. Such a model is applicable when the timescale of plume formation is shorter than the ascent time of the plume, better representing the formation of small discrete plumes. Results well reproduce the characteristics of the plume with height. Application of both types of one-dimensional models requires the assumption that the gas and particle phases are well mixed, in thermal equilibrium, and that the mixture is just buoyant relative to the atmosphere [*Woods and Wohletz*, 1991].

More complex multidimensional transient models have also been applied to the coignimbrite plume problem. The studies of *Neri et al.* [2002] and *Neri et al.* [2003] describe explicitly the multiparticle nature of the flow and investigated the properties (mass and grain size) of the material lofting to form coignimbrite plumes. *Herzog and Graf* [2010] apply the ATHAM model, which takes into account complex microphysical processes within the plume, and highlight the complications that arise in modeling plumes that loft from multiple and extended source regions, and the limitations in applying one-dimensional models to such plumes, specifically when assessing the neutral buoyancy level. However, such three-dimensional models are computationally expensive, and therefore, statistical investigation of modeled plume characteristics from uncertain input conditions is difficult.

In the study presented here, we implement and couple the steady state models of *Bursik and Woods* [1996] and *Bursik* [2001], representing ash flow propagation and plume rise, respectively, to investigate the conditions required for coignimbrite plume formation and, once formed, the maximum height attained by the resultant plume. Both the ash flow and plume model are 1-D axisymmetric steady state, and application is assumed to be valid in the case that flow emplacement time is on the order of hours, deposition occurs from the sustained flow [*Bursik and Woods*, 1996], and that plume rise occurs over shorter timescales than plume liftoff. We also apply global sensitivity analysis using DAKOTA software [*Adams et al.*, 2009] to provide a statistical assessment of the key dependencies of both models.

2. Numerical Models

2.1. Ash Flow Model

A modification of the depth-averaged ash flow model of *Bursik and Woods* [1996] is employed to simulate the propagation of turbulent, dilute (characterized by initial mixture densities of less than 20 kg/m^3) currents, which form as a result of column collapse (Figure 1). As a consequence of cooler ambient air entrained into the collapsing column, the initial temperature of the propagating current is less than that of the erupted material. The model solves equations for conservation of mass (for both mixture and particles of different sizes), momentum, and energy (equations are presented in Appendix A). In addition to the original model, transport equations are also solved for specific heat and gas constants of the mixture with distance, changing with distance because of particle sedimentation and entrainment of atmospheric air. The model assumes that the particles and gaseous phases are in thermal equilibrium and that they have the same horizontal velocity. The vertical velocity is assumed to be negligible for the gas phase, and equal to the settling velocity for the particulate phase, thus leading to deposition. It is assumed that the flow is incompressible and flow characteristics are depth averaged; i.e., density dishomogeneity is not taken into account. Such an assumption is valid here if it is assumed that we are either modeling only very dilute ash flows or that we are only considering the turbulent upper portions of a propagating sedimenting current.

Both particle sedimentation and entrainment of ambient air are crucial for modeling changes in flow density with distance from source. *Valentine* [1987] showed that particles with a Rouse number P ($P = v_{s,i}/v_{\mathrm{RMS}}$, where v_{RMS} is the root-mean-square of turbulent velocity fluctuations in the mixture) less than 2.5 (i.e., less than a centimeter) form a stratified turbulent flow whereby sedimentation rate is dependent on the vertical concentration profiles of particles in the flow. Estimation of the turbulent velocity fluctuations of the mixture cannot be estimated by application of the one-dimensional model, and therefore, the Stokes number of the particles used herein is not defined. For simplicity, the model assumes that the particles are homogeneously distributed across the thickness. Here the initial particle grain size distribution is considered to have a unimodal distribution and is partitioned into discrete bins with diameter D_i, $i = 1, \ldots, n$. Following *Bursik and Woods* [1996], sedimentation rate S_i of each particle class is dependent on the particle settling velocity $v_{s,i}$, whereby

$$v_{s,i} = \sqrt{\frac{\varrho g D_i}{C_d \rho_m}}, \tag{1}$$

and

$$S_i = \frac{M_i v_{s,i}}{hu}, \tag{2}$$

where ϱ is the particle density, g is gravitational acceleration, C_d is the particle drag coefficient (equal to 1 as in *Bursik and Woods* [1996]), ρ_m is the flow density, M_i is the mass flux of the particles with diameter D_i, h is flow thickness, and u is flow velocity.

The flow Richardson number, describing the ratio of buoyant to turbulent forces, is key for defining entrainment efficiency and flow type:

$$Ri = \frac{gh(\rho_m - \rho_a)}{\rho_m u^2}, \tag{3}$$

where ρ_a is the density of the ambient. Within the ash flow model, entrainment is only modeled at the upper surface of the flow. While effects of entrainment at the lateral edges are important in the case of one-dimensional currents in Cartesian coordinates, this is not true for the axisymmetric geometry investigated here. Following *Bursik and Woods* [1996] and *Parker et al.* [1987], entrainment ε can be calculated empirically as

$$\varepsilon = \frac{0.075}{\sqrt{1 + 718 Ri^{2.4}}}. \tag{4}$$

Therefore, entrainment is considerably more efficient at low Richardson numbers. *Bursik and Woods* [1996] describe two flow end-member types, defined by their Richardson number: supercritical ($Ri < 1$) and subcritical flow ($Ri > 1$). Supercritical flows are described as thin and fast, with efficient entrainment resulting in increased particle settling velocities and therefore sedimentation rate due to a reduction of the mixture density. In comparison, subcritical flows are slow moving and thick, entraining little ambient air during propagation. In nature, subcritical flows occur upstream of a topographic barrier [*Levine and Kieffer*, 1991] or

Table 1. Parameter Bounds for Initial Conditions Used for Application of the Ash Flow Model, Relating to Mass Flow Rates of Between 10^8 and 10^{10} kg/s[a]

			Sensitivity Indices			
			Liftoff Distance		Plume Height	
Parameter	Minimum	Maximum	Main	Total	Main	Total
Flow thickness (km)	0.25	2	0.170	0.236	0.353	0.416
Flow radius (km)	0.25	2	0.315	0.389	0.176	0.177
Richardson number[b]	0.1	0.99	−0.00035	0.0047	0.07	0.08
Gas mass fraction	0.1	0.3	0.253	0.365	0.14	0.17
Temperature (K)[c]	800	1100	0.144	0.141	0.042	0.08
Friction[d]	0.001	0.02	0.003	0.003	0.0002	0.00008
Median phi	−3.0	3.0	0.005	0.01	−0.0009	0.0002

[a]Initial flow velocity is calculated as a function of the Richardson number and flow height and ranges between 20 and 280 m/s. Initial magmatic gas mass fraction is 0.03 throughout. Main and total sensitivity indices for liftoff distance and plume height as discussed in section 3.
[b]*Bursik and Woods* [1996].
[c]*Sparks et al.* [1997].
[d]*Schlicting* [1969].
[e]*Sparks et al.* [1978].

associated with decreasing velocity related to radial spreading or high basal friction. As shown in *Bursik and Woods* [1996], in comparison with subcritical flows, supercritical flows have much smaller liftoff distances due to higher velocities and more efficient entrainment of ambient air, allowing buoyancy reversal to be achieved earlier and depositing a much smaller fraction of erupted ash (in spite of the larger sedimentation rate). Transition from supercritical to subcritical flow occurs via a hydraulic jump, where the Richardson number goes from below to greater than 1, associated with a sudden decrease in flow velocity accompanied by an increase in flow thickness. The conditions required for hydraulic jumps are difficult to constrain and validate and go beyond the scope of this study, and therefore, herein, only supercritical flows are considered.

In comparison to the model presented in *Bursik and Woods* [1996], for this study the terms of the equations were rearranged such that the initial velocity u is calculated as a function of the initial Richardson number:

$$u = \sqrt{\frac{(\rho_m - \rho_a)gh}{Ri\rho_m}} \tag{5}$$

allowing only solutions in the supercritical regime to be modeled. As a consequence, the model input parameters are as follows: initial flow thickness and radius, Richardson number, temperature, gas mass fraction, and the characteristics of particles within the flow. In Table 1, parameter bounds for each input are provided, resulting in a range of mass flow rate between 10^8 and 10^{10} kg/s. We assume that the flows are propagating across a flat plane, a valid assumption given that modeled runouts are on the order of many kilometers.

The equations of *Bursik and Woods* [1996] are solved by a predictor-corrector integration scheme, with flow parameters calculated as a function of distance. The liftoff distance (assumed by *Bursik and Woods* [1996] as the final runout of the flow) is defined as the distance at which the flow density reaches ambient and is assumed to represent the initial radius of the lofting coignimbrite plume (i.e., lofting occurs from the entire current extent). A number of flow characteristics are extracted at this distance from the flow model solution, for example, flow temperature, gas mass fraction, velocity, and mass flow rate, to provide insight into the process of coignimbrite plume formation and constrain characteristics of the mixture at liftoff. The final flow mass flux M, the final radius r, and the final density ρ_m (corresponding to the condition of neutral buoyancy) are used to calculate the initial upward plume velocity u_p by

$$u_p = \frac{M}{\rho_m \pi r^2} \tag{6}$$

This simplified assumption is based on observations of the Mount St. Helens 1980 eruption which show that lofting occurred from the entire area inundated by the PDC [*Sparks et al.*, 1986] and 2-D/3-D model results

which show that lofting initially occurs in localized areas and then extends to the whole PDC inundation area [*Esposti Ongaro et al.*, 2012]. For a given mass flux M, the velocity estimated in equation (6) from the PDC inundation area is a minimum value with respect to a more localized plume source.

2.2. Plume Model

A modified version of the *Bursik* [2001] steady state plume model was applied to study the relation between source conditions and plume characteristics. The plume model from VOL-CALPUFF [*Barsotti et al.*, 2008; *Barsotti and Neri*, 2008] solves in an Eulerian framework the equations for conservation of mass, momentum, and thermal energy of bulk mixture with height (see Appendix B for equations) and, like the flow model, assumes that the mixture is in thermal equilibrium. The model is capable of taking into account both radial entrainment α, by development of turbulent eddies at the plume edge, and that from wind β. In the examples presented here, plume rise is assumed to occur under low wind conditions, and therefore, only radial entrainment is accounted for. Particle loss is assumed to occur from the edges of the column only, and the probability of particle sedimentation is a function of particle settling velocity and radial entrainment. Re-entrainment of particles is assumed to be negligible and is not considered within the model.

Results from application of one-dimensional plume models have been found particularly dependent on entrainment coefficient [*de' Michieli Vitturi et al.*, 2016; *Costa et al.*, 2016]. Entrainment coefficient is an important consideration for coignimbrite plumes with *Calder et al.* [1997] noting that constant entrainment with height, as applied by *Woods and Wohletz* [1991] following the assumption that the size of turbulent eddies scale with plume radius, is not realistic because of the sharp and nonlinear change in plume radius and vertical velocity near source. Application of such an entrainment assumption results in a nonhomogeneous plume with the edges being well mixed compared to the plume center [*Calder et al.*, 1997], forming a core which is hotter and has a higher solid mass fraction than the plume edges. Accurate representation of such complex plume structure is not possible with integral models [*Costa et al.*, 2016]; however, *Calder et al.* [1997] apply an altitude-dependent entrainment law to investigate the effect of less efficient entrainment in the lower regions of the plume. Here we achieve the same reduction in entrainment at lower levels in the plume by application of the *Carazzo et al.* [2008] entrainment assumption.

In contrast to the studies of *Barsotti et al.* [2008], *Bursik* [2001], and *Woods and Wohletz* [1991], where constant entrainment with height is assumed, here entrainment is calculated as a function of the plume Richardson number following *Carazzo et al.* [2008, and references therein]. The application of a variable coefficient results in reduced entrainment when the plume density is greater than that of the ambient, while greater entrainment occurs when the density of the plume is less than that of the ambient. Therefore, in the coignimbrite example, where the initial density is equal to ambient, entrainment increases with height within the first few kilometers as the density difference between the rising mixture and ambient increases, similar to the entrainment assumption applied by *Calder et al.* [1997], and then decreases as the plume approaches neutral buoyancy level. Entrainment is considerably less at lower levels for the Plinian plume, because the initial plume density is greater than that of the ambient, before increasing and decreasing in a similar manner to the coignimbrite example. This difference means that the coignimbrite plume entrains more ambient air than the Plinian plume for the same mass flux.

Required input parameters for the plume model are gas mass fraction, temperature, velocity, and radius of the lofting plume. In all examples, the starting density of the mixture was assumed to be neutral, i.e., equal to ambient. The initial radius, velocity, and temperature ranges of the lofting mixture were defined by the 5th to 95th percentiles of the values at the final liftoff distance from the ash flow model, with a uniform distribution assumed (Table 2).

2.3. Coupled Model

The ash flow and plume model were coupled, with a number of ash flow model outputs used as inputs to the plume model (Figure 2). Coupling of the models requires a number of assumptions: the flow liftoff distance is equal to the initial plume radius, all unsedimented particles are lofted into the plume, and finally, the initial vertical velocity of the rising plume is controlled by the mass flow rate of the current (as described in equation (6)). The input parameters for the coupled simulations are the same as those used in application of the ash flow model (Table 1).

2.4. Sensitivity Analysis

Global sensitivity analysis was performed using the software DAKOTA [*Adams et al.*, 2009], whereby the input parameter space is explored with Latin hypercube sampling such that input-output parameter interactions

Table 2. Range of Values Used for Application and Sensitivity Analysis of the Plume Model for the Maximum Plume Height and Neutral Buoyancy Level[a]

				Sensitivity Indices	
Parameter	5th Percentile	Median	95th Percentile	Maximum Plume Height	Neutral Buoyancy
Initial radius (km)	1.5	3.8	8.7	**0.635**, *0.667*	**0.581**, *0.610*
Velocity (m/s)	8.9	23.5	52.6	**0.206**, *0.217*	**0.271**, *0.275*
Temperature (K)	635.6	765.2	904.6	**0.14**, *0.137*	**0.134**, *0.129*

[a]Input values correspond to the 5th and 95th percentiles of the output values from the ash flow model by assuming the input ranges of variables reported in Table 1. In the examples presented here, equations are solved with a predictor-corrector integration scheme. Integration ceases when the vertical plume velocity is equal to zero, defining the maximum plume height. The neutral buoyancy height, the height at which the plume intrudes laterally into the atmosphere, is not explicitly evaluated in the model. However, the neutral buoyancy height is estimated as the height at which the mixture density is equal to that of the atmosphere. Main sensitivity indices are in bold, and total sensitivity indices are in italics.

are quantified statistically using a variance-based decomposition method. Application of sensitivity analysis requires identification of a valid distribution (in the examples a uniform distribution is assumed) of values for each input parameter. The numerical model is applied a number of times while varying input parameters by sampling the ascribed distribution for each parameter. The sensitivity of model results to model inputs is depicted by Sobol indices which describe the fraction of the variation in model output that can be attributed to each input. Two measures are presented here, the first, main sensitivity indices (S_i):

$$S_i = \frac{\mathrm{Var}_{x_i}[E(Y|x_i)]}{Var(Y)} \tag{7}$$

which correspond to the fractional contribution of the input variable x_i to variance of the model output Y, allowing identification of the input variables with the most effect on the model output. The second, total sensitivity indices T_i, where

$$T_i = \frac{E(\mathrm{Var}(Y|x_i))}{\mathrm{Var}(Y)} = \frac{\mathrm{Var}(Y) - \mathrm{Var}(E[Y|x_{-i}])}{\mathrm{Var}(Y)} \tag{8}$$

where $Y = f(x)$ and $x_{-i} = (x_1, \ldots, x_{i-1}, x_{i+1}, \ldots, x_m)$, $\mathrm{Var}(Y)$ is the variance in the model output and E denotes the conditional expectation. The main sensitivity index S_i quantifies the expected reduction in variance in the model output that would be achieved if the input x_i were fixed [*Saltelli et al.*, 2008]. The total sensitivity indices T_i describe both the relation of the final model output to the input x_i and also the interaction of the parameter of interest with other input parameters. In both cases, a larger index implies a greater reliance of the output on the input parameter.

3. Results

3.1. Ash Flow Model

Figure 3 illustrates the radial behavior of a few key flow variables—flow thickness, velocity, temperature, density, sedimentation, and entrainment rate—for three selected simulations where only the initial Richardson number is varied. Analysis of equation (3) shows that varying the initial Richardson number results in different initial flow velocities and consequently entrainment efficiency. All simulations initiate with a thickness of

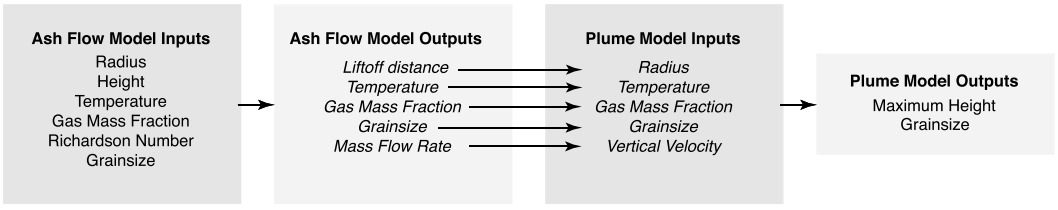

Figure 2. Flow diagram illustrating the key inputs and outputs from the ash flow and plume models. Further details in text.

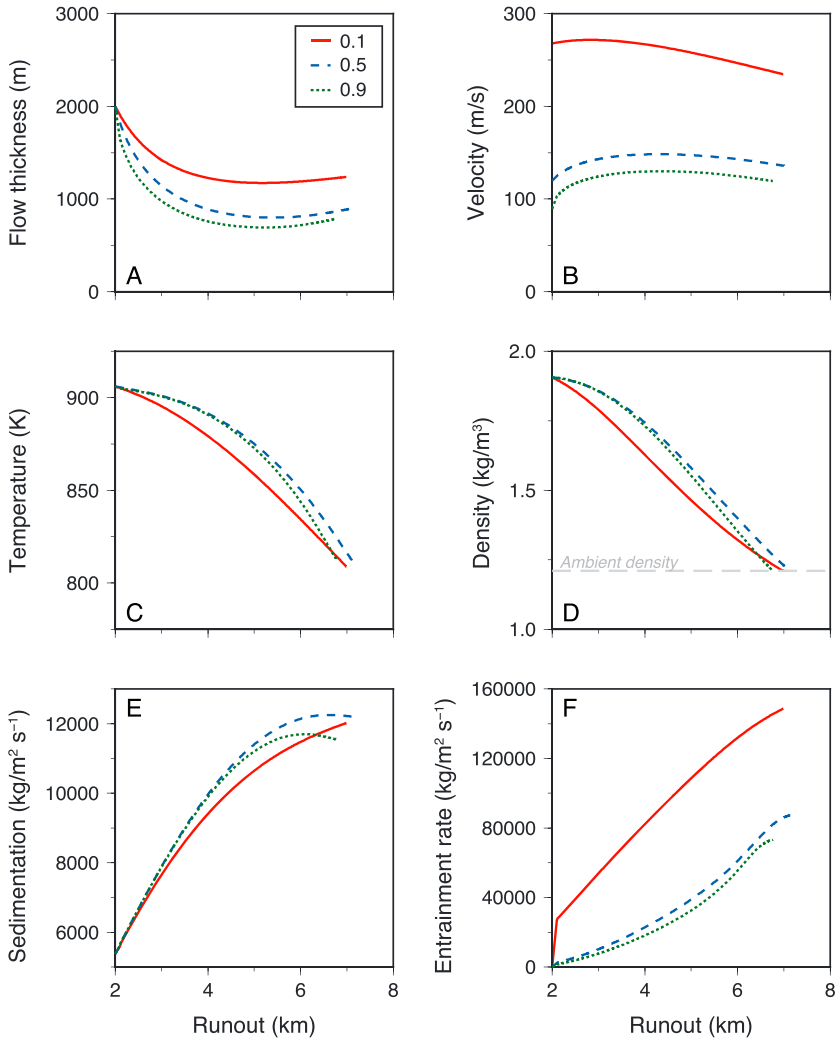

Figure 3. Profiles of selected flow characteristics, flow (a) thickness, (b) velocity, (c) temperature, (d) density, (e) sedimentation rate, and (f) entrainment rate with distance from source for three different axysymmetric simulations, spanning the supercritical flow regime. The solid red, dashed blue, and dotted green lines correspond to calculations made at $Ri = 0.1$, 0.5, and 0.9, respectively. In Figure 3d, the grey dashed line denotes ambient density (1.225 kg/m^3). Initial flow thickness and radius of 2 km, initial gas mass fraction is 0.2, initial temperature of 900 K, and a friction coefficient of 0.001 were used. A grain size distribution with a median grain size and standard deviation of 1 phi is applied (see Figure S1). Note that despite similar liftoff distances, the initial mass flow rates of the currents are very different (10^9 – 10^{10} kg/s), with a lower *Ri* number corresponding to larger mass flow rates.

2 km. In each example, the model predicts an immediate reduction in thickness, followed by a relatively constant thickness until final liftoff distance. The flow with the lowest initial Richardson number is thickest, related to greater entrainment of air as evidenced by lower flow density than the other examples (Figure 3).

The velocity profiles vary significantly for each example, as initial velocity is controlled by the input Richardson number. In all of the examples, there is an initial increase in flow velocity related to the sudden reduction in flow thickness, followed by a small decrease as the density difference between the propagating current and ambient reduces. The final velocity for each example is greater than 100 m/s at the point at which flow density becomes equal to atmospheric (1.21 kg/m^3).

Each simulation initiates with an eruption temperature of 1000 K, approximately equating to an initial flow temperature of 900 K once entrainment during column collapse is accounted for. Over the propagation, flow temperature decreases by 100 K in all examples, but at different rates associated with varying entrainment efficiencies. Similar patterns are seen in flow density profiles. Despite the same initial and final densities, density profiles vary as a function of Richardson number, with the mid-Richardson number simulation density

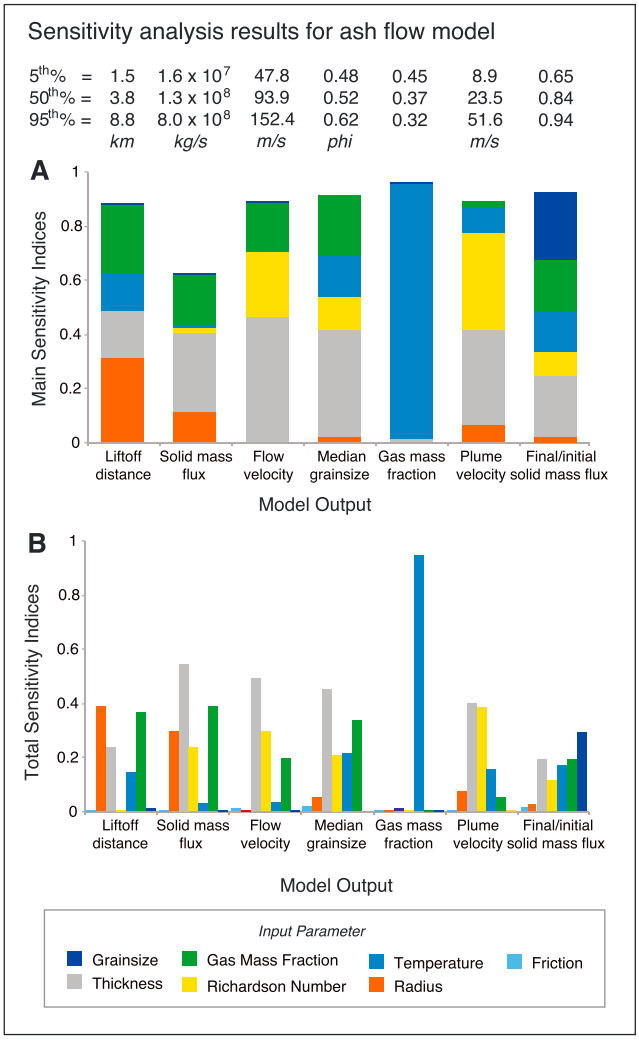

Figure 4. Sensitivity indices for ash flow model from 2000 simulations, quantifying the relative weight of input parameters on ash flow model outputs at final runout for the range of input parameters provided in Table 1. (a) Main sensitivity indices identifying the input variables with greatest effect on model output. (b) Total sensitivity indices describing relation between model input and output and also interaction of the parameter with other input parameters.

decreasing at a slower rate compared with the other simulations, due to reduced entrainment and therefore decreased sedimentation of particles (see equation (1)). While the other flow parameters vary at the liftoff distance, the final temperature and density are the same for each of the simulations, relating to the liftoff condition, whereby flow propagation ceases once density reduces to that of the ambient. Despite the different initial Richardson numbers, and consequently initial velocities and mass flow rates (between 4×10^9 and 10^{10} kg/s), the liftoff distance for each example is similar, between 7 and 8 km.

Multiparametric sensitivity analysis was conducted to quantify the relation between input parameters and final flow characteristics, as described above. In Figure 4, the histograms report the main and total sensitivity indices as computed by the global sensitivity analysis. The liftoff distance, calculated as the distance at which the mixture density is equal to ambient, is dominantly controlled by the variability in the initial radius and gas mass fraction, while the initial flow thickness and temperature have a smaller effect. The results show a range of liftoff distances, with those from runs with a mass flux of 10^9 kg/s the same as those in *Bursik and Woods* [1996]. The final solid mass flux, which describes the amount of particles available to feed the coignimbrite plume, is dominantly controlled by the initial flow thickness but is also a function of the initial gas mass fraction and radius. The final flow velocity is a function of initial flow thickness, Richardson number, and gas mass fraction. The final grain size is a function of the initial flow thickness, gas mass fraction and temperature (which together describe the flow density), and the initial Richardson number, which controls the initial

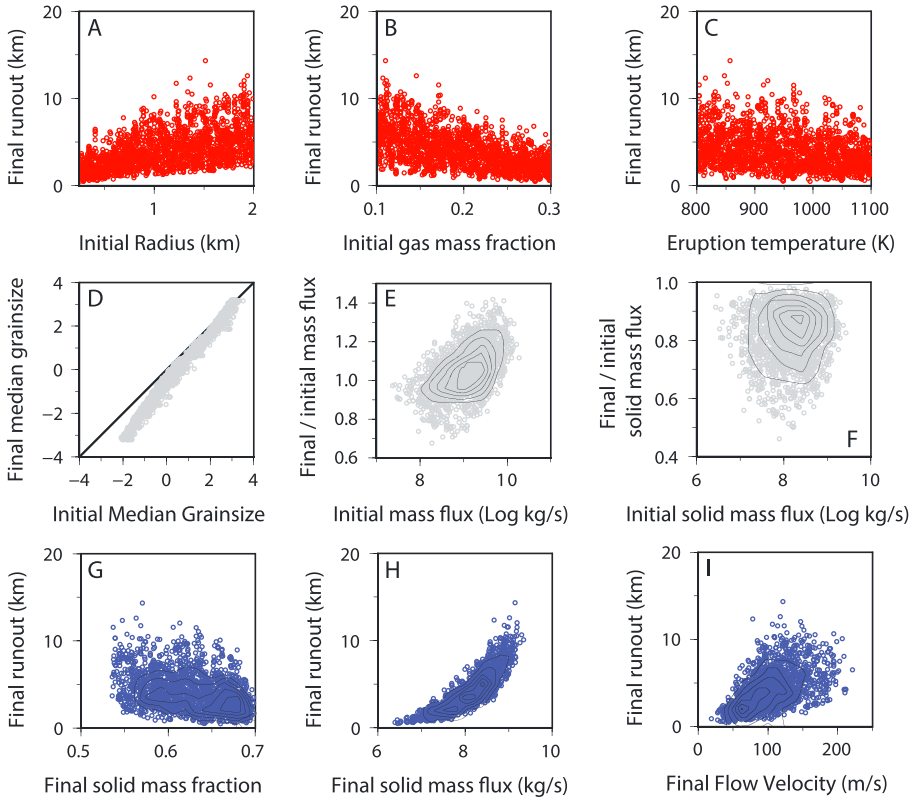

Figure 5. Sensitivity analysis results from 2000 simulations displaying the relation of various flow parameters to input parameters (red) and the correlation between runout distance and flow parameters at liftoff (blue). Each marker represents the result from one simulation. Range of input parameters in Table 1. In contrast to simulations used for the sensitivity analysis presented in Figure 4, here the initial grain size distribution has a median of 0 phi (1 mm) and a standard deviation of 2 phi. Contours represent density of the points.

flow velocity; however, the variability in final median grain size is minor. The relation between initial temperature and final gas mass fraction is again related to the final condition of neutral density, and consequently, final gas mass fraction is almost solely controlled by initial temperature. The initial plume velocity is calculated from the flow mass flux at liftoff (equation (6)) and therefore is largely dependent on initial Richardson number, which describes initial flow velocity, and initial flow thickness, while initial temperature and radius also play a role. The final to initial solid mass flux ratio shows that the amount of material that remains in the flow at the liftoff distance is controlled by the input grain size, initial flow thickness, Richardson number, temperature, and gas mass fraction (see Figure S2 in the supporting information). Apart from the solid mass flux, the sum of the main indices for the other model outputs is close to 1, meaning that there is little interaction between input parameters controlling the output results. The total sensitivity indices (Figure 4b) show that the Richardson number interacts with the initial height, radius, and gas mass fraction resulting in variability of the solid mass flux.

While application of sensitivity analysis enables identification of the key parameters for model results of interest, it does not provide any information on the type of relation between input parameter and model output and on the range of output values. In Figure 5, the liftoff distance from each of the simulations is presented versus the controlling input parameters as determined from the whole set of runs (2000 simulations) performed for the sensitivity analysis. There is a positive correlation between initial radius and the liftoff distance (Figure 5a), while the relation between the initial gas mass fraction (Figure 5b) and temperature (Figure 5c) is negatively correlated. There is a greater spread in liftoff distance for a given temperature, compared to the range for a given initial radius or gas mass fraction, resulting in a lower sensitivity indices (Figure 4 and Table 1).

For insight into how the modeled liftoff distance correlates with the grain size of material available for the buoyant plume, the final median grain size is shown against the initial median grain size (Figure 5d). A line

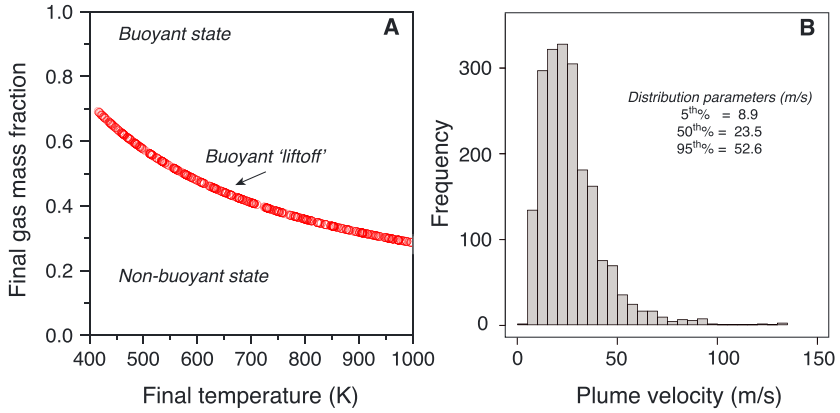

Figure 6. Characterization of key flow parameters at coignimbrite plume formation, (a) buoyant plume formation controlled by mixture temperature and gas mass fraction and (b) calculated vertical velocity. Figure 6a shows buoyant plume formation controlled by a balance between flow temperature and gas mass fraction. The buoyant liftoff condition follows a power law. Figure 6b shows distribution of initial plume vertical velocities calculated from distribution of final mass flow rates of the PDC at liftoff.

representing equal initial and final median grain size is also shown. The results show that for coarser particles, the difference in grain size between flow initiation and plume formation is greater, with the median grain size at distance being finer. This difference is only minor, however, with a difference of the order of 1 phi for an initial median diameter of −3 phi. The difference between initial and final median grain size decreases with finer median grain size, with the results converging on the line of equal initial and final median grain size. These results are consistent with those of *Bursik and Woods* [1996] over the same runout distances.

The range of initial mass flux (10^8 to 10^{10} kg/s) utilized in the simulations represents a range of eruptive sizes. In the majority of the simulations, the final to initial mass flux ratio is greater than 1 (Figure 5e), indicating that the final mass flux is greater than the initial mass flux, due to entrainment of ambient air and comparatively little sedimentation. The same plot for the solid mass flux is much less clear and does not show a clear relation (Figure 5f). While the correlation is not distinct, flows with greater liftoff distances have a lower final solid mass fraction (Figure 5g), due to the entrainment of ambient air. There is a strong correlation between the liftoff distance and the final solid mass flux (Figure 5h), with the final solid mass flux much larger for flows with greater liftoff distances. These results show that larger flows produce larger coignimbrite plumes, due to greater initial mass flux. The flow profiles displayed in Figure 3b show high final velocities at liftoff. Results from the multiparametric studies show a large range in final radial velocity (Figure 5i), from a few m/s to a hundred m/s, with a positive correlation between final flow velocity and final runout.

The sensitivity analysis results presented in Figure 4 show that the final gas mass fraction (i.e., the source gas mass fraction of the coignimbrite plume) is controlled by the eruptive temperature alone. To investigate this relation further, the gas mass fraction and temperature of the ash flow at neutral buoyancy were plotted for each of the simulations presented in Figure 5. The resultant graph (Figure 6a) depicts two regions, one where the mixture is buoyant and one where the mixture is too dense to rise, and therefore, flow continues. The two conditions are separated by a power law relation, $(n = f(T) = 291.1T^{-0.97}$, where n is the final gas fraction and T is the final temperature, (K)), representing the equation of state. This plot reiterates results in Figure 3 where the temperature decrease is the same for all simulations despite different liftoff distances, as initial flow density, a function of initial gas mass fraction and temperature are the same, and therefore, lofting conditions are also the same.

Estimates of vertical velocity determined from the final mass flux of the flow (calculated from equation (6)) are considerably larger than those previously described in the literature. Vertical velocity was calculated for each of the simulations in Figure 5 and are plotted as a histogram in Figure 6b. The calculated velocities follow a lognormal distribution, with 95% of the calculated velocities less than 51.3 m/s, and a mode of 20 m/s. As mentioned above, these values are calculated assuming that the plume lofts from the entire extent of the flow and also that the flow horizontal velocity instantly changes to vertical velocity.

Table 3. Inputs Used and Resultant Maximum and Neutral Buoyancy Heights for Plume Profiles Shown in Figure 7 for a Mass Flow Rate of 10^7 kg/s

Simulation and Entrainment Assumption	Initial Radius (km)	Initial Velocity (m/s)	Initial Temperature (K)	Initial Density (kg/m^3)	Maximum Plume Height (km)	Neutral Buoyancy (km)
Vent derived, constant	100	300	1100	0.20E+02	27.381	18.800
Vent derived, variable					20.284	14.750
Coignimbrite, constant	1555	20	832	0.12E+01	25.243	17.630
Coignimbrite, variable					22.271	15.289

3.2. Plume Model

A number of differences exist between Plinian and coignimbrite plume source conditions. In Plinian plumes, the source area is small, the density of the mixture is considerably greater than the ambient, and the initial vertical velocity is on the order of hundreds of m/s (without considering the likely overpressured condition of the eruptive mixture at the vent exit). In comparison, coignimbrite plumes loft from a much larger area, have a similar density to the ambient, and have smaller vertical velocities. In order to highlight the differences, we conducted two sets of simulations (one for the vent-derived plume example and one for the coignimbrite) using the plume model, to compare plume characteristics with height given the different source characteristics, assuming an initial flow rate of 10^7 kg/s in both cases. To achieve the initial flow rate, the initial radius of the coignimbrite plume is an order of magnitude greater than that of the vent-derived plume, while both the density and the initial velocity are an order of magnitude less (input parameters are provided in Table 3). For both plume types, simulations with two entrainment coefficient assumptions were conducted, the first assuming constant entrainment coefficient (0.09 following *Morton et al.* [1956]) with height and the second with a variable coefficient, following *Carazzo et al.* [2008]. Comparison of modeled plume radius, velocity, and density with height for the coignimbrite and vent-derived plumes (Figure 7) shows a number of differences both in profiles with height and also the maximum plume height. Specifically, the radius of the vent-derived plume increases with height, while the radius of the coignimbrite plume initially decreases, before following similar trends to the vent-derived plume and increasing with height. The density of the vent-derived plume is initially much greater than ambient, but the plume becomes buoyant within the first few kilometers. The vent-derived example with variable entrainment attains buoyancy at greater altitudes than the constant entrainment example. The starting condition of coignimbrite plume simulations is neutral buoyancy, and in comparison to the vent-derived results, there is very little difference in density trends with height for the two entrainment assumptions. The variable entrainment coefficient simulation results are density dependent, with reduced entrainment when the plume density is greater than ambient. In all cases, the plume density becomes equal to and then larger than ambient density at height in the atmosphere but before the maximum plume height (determined as the point at which the vertical velocity is zero) is reached. This transition represents the numerical neutral buoyancy level (Table 3) and is assumed to be the height at which lateral intrusion of the plume occurs.

In comparison to plume radius and density, there are significant differences between velocity profiles both with plume type and entrainment assumption. The initial vertical velocity of the vent-derived plume is large and reduces drastically in the first few kilometers. Application of the two entrainment conditions results in different plume profiles for the vent-derived plume example. Where the constant entrainment coefficient is used, the plume velocity shows a decrease with altitude (simple buoyant), while when the variable entrainment coefficient is used, the plume is superbuoyant (whereby the plume velocity decreases and then increases with height) [*Bursik and Woods*, 1991]. The velocity of the coignimbrite plumes increases more gradually with height, with significant deviation between the simulations with different entrainment assumptions occurring above an altitude of approximately 5 km.

For both plume types, the plume height attained using the constant entrainment coefficient assumption is considerably greater than that for the variable entrainment coefficient. The modeled results show that maximum plume height is not simply a function of initial mass flux. Here where the variable entrainment coefficient is used, the coignimbrite plume is modeled to reach a greater height than that of the vent-derived plume, despite the same initial mass flux because the entrainment coefficient is larger for centrally buoyant plumes.

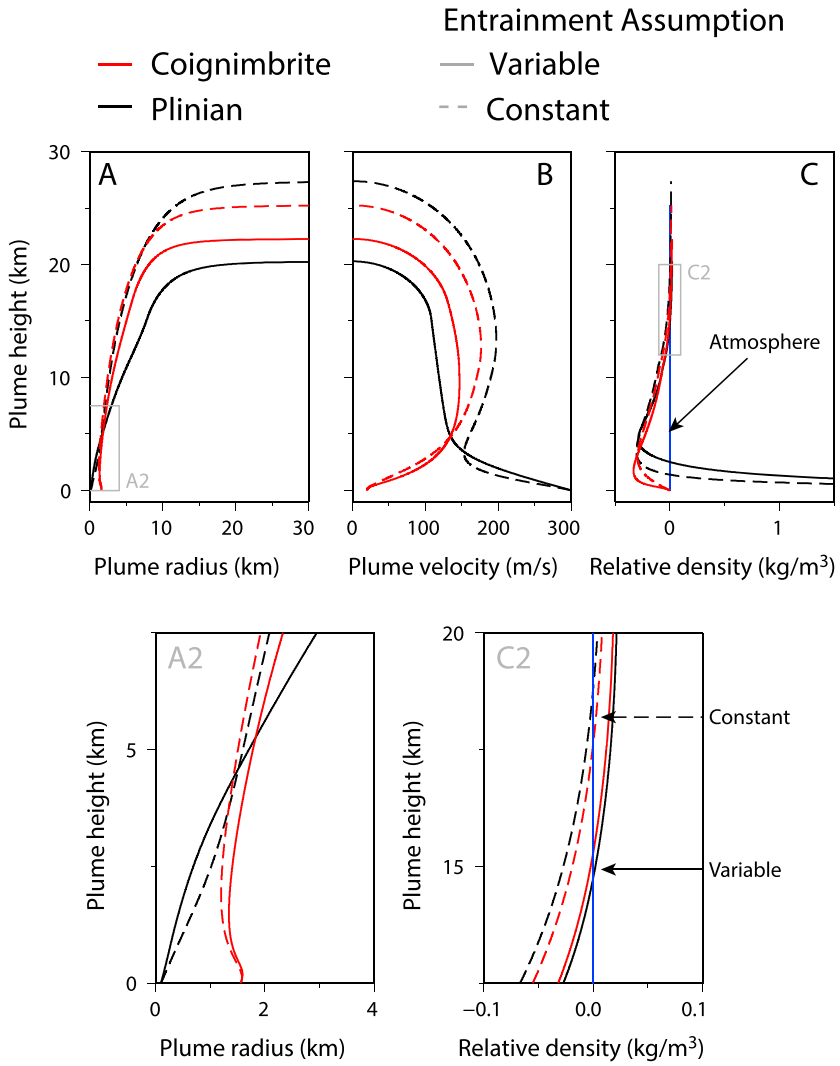

Figure 7. Typical plume profiles for a vent-derived and coignimbrite plume example with the same initial mass flow rate (10^7 kg/s) and for two different entrainment assumptions: constant with height following *Morton et al.* [1956] and variable with height following *Carazzo and Jellinek* [2012]. (a) Plume radius with height with A2 showing variation in plume radius close to source. (b) Plume velocity with height. (c) Plume density with height. Standard atmospheric density profile also shown for comparison. C2 shows the point at which neutral buoyancy is reached, with the solid arrow displaying height for variable entrainment solutions and the dashed arrow height for constant entrainment solutions (Table 3).

Multiparametric sensitivity analysis was also applied to the plume model using the variable entrainment assumption, with the output of interest being the maximum plume height (Figure 8a). Previous modeling results using one-dimensional models show that under the assumption of negligible aggregation and fragmentation processes, there is little change in modeled grain size from the base to the top of the plume [*de' Michieli Vitturi et al.*, 2015]. Sensitivity indices determined here show that the main control on modeled plume height is the initial plume radius, with initial vertical velocity and temperature playing a lesser role. Analysis of modeled maximum plume height versus initial radius and velocity, describing the mass flow rate, and temperature, describing buoyancy, shows a distinct positive correlation (Figure 8b), with the maximum modeled plume height increasing with an increase in each input.

3.3. Coupled Model Results

The ash flow and plume were coupled to investigate controls of initial PDC characteristics to those of the coignimbrite plume. A variable entrainment coefficient was assumed for the plume model, and output parameters from the ash flow model were either used directly or to infer inputs for the plume model (Figure 2).

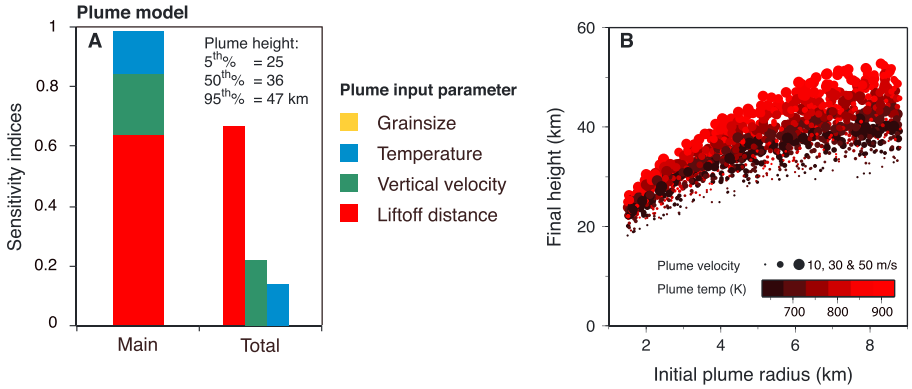

Figure 8. (a) Sensitivity analysis for plume model and (b) model results identifying key controls on modeled maximum plume height. Figure 8a shows sensitivity analysis results for coignimbrite plume height based on plume source conditions. In Figure 8b each marker represents the result from one simulation where the marker size corresponds to the initial plume velocity, while the color corresponds to initial plume temperature. Range of input parameters for plume model in Table 2.

Multiparameter sensitivity analysis results indicate that the controlling parameters on modeled plume height are the initial flow thickness, radius, and gas mass fraction, in decreasing order of importance, with temperature and Richardson number having a minor effect (Figure 9a). This result is unsurprising given that the initial plume velocity is calculated from the final mass flow rate of the flow, a function of the flow density (controlled by mixture gas mass fraction and temperature), velocity (determined by input Richardson number), and radius. Further analysis of the simulation results (Figure 9b) shows a positive correlation between maximum plume height and initial flow radius but a negative correlation with initial Richardson number and gas mass fraction.

4. Discussion

The liftoff distance is used to infer the approximate location of and the conditions required for coignimbrite plume formation. The relation between initial radius, controlling initial mass flow rate, and liftoff distance is linear, with liftoff distance simply increasing with the initial radius. As such, this result does not reflect processes occurring within the flow but instead, in combination with the initial thickness, describe the initial mass flux of the flow. Liftoff distance and coignimbrite plume formation are controlled by both flow temperature and gas mass fraction, which together determine flow density. The results presented herein indicate that flows with a higher initial temperature have a shorter runout, and coignimbrite plume formation occurs closer to vent. The higher temperatures also mean that the mixture can become buoyant at higher particle concentrations, and therefore, hotter flows can supply larger amounts of particles to coignimbrite

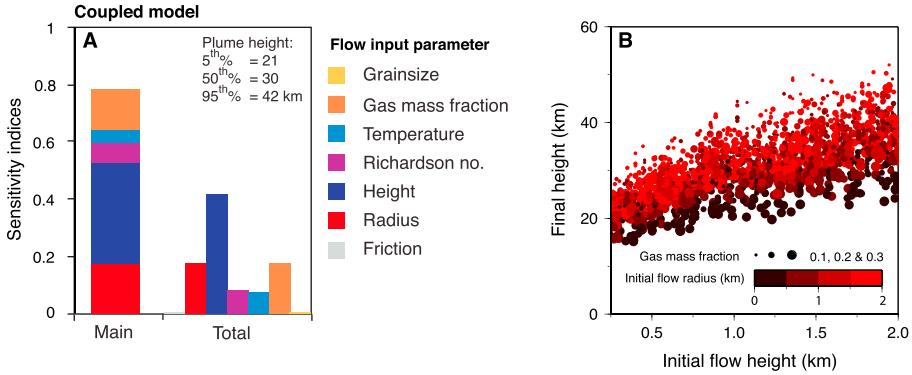

Figure 9. (a) Sensitivity analysis for the coupled model and (b) model results showing sensitivity of coignimbrite plume height on PDC input conditions. In Figure 9b marker size relates to flow initial gas mass fraction, while color relates to initial flow radius. Range of input parameters for the coupled model is the same as those used for the ash flow model (Table 1.)

plumes than cooler flows. *Andrews and Manga* [2012] also showed this relation in experiments of coignimbrite plume formation.

While our results are consistent with those of *Bursik and Woods* [1996], it is important to note that in this study we only account for radial supercritical flows. Compared to subcritical flows, supercritical flows have shorter runout distances, meaning less material is deposited and more material is available for lofting into the plume. The assumption of radial flow further reduces the runout distances, and consequently, a much smaller mass of ash is deposited with respect to directed flows. The ash flow model does not take into account a number of processes or interactions that would affect plume formation. Specifically, our model (following *Bursik and Woods* [1996]) assumes that the entrainment coefficient varies across the flow as the flow Richardson number changes. We also assume that entrainment in the flow does not vary once plume formation has occurred, inherent in the steady state assumption of the model. Observations from experiments [*Andrews*, 2014] indicate that once the coignimbrite plume forms, the upper surface of the current is unable to efficiently entrain air, leading to a reduction in entrainment rate. However, experiments of plume formation [*Andrews and Manga*, 2012] show that the lofting of the plume also leads to increased air entrainment at the current margins. While it is possible to model the transition in entrainment states, and lateral entrainment into current using three-dimensional models, it is not possible to account for these complexities using a one-dimensional axisymmetric model.

The model applied here assumes sustained plume formation, i.e., that the time taken for plume formation is less than the rise height of the plume. Such an assumption is thought to be valid for large ignimbrite-forming eruptions, with large initial mass flux rates whereby the flows are fed by a collapsing column. Examples of such events are thought to include the Campanian Ignimbrite and the Bishop Tuff eruptions [*Bursik and Woods*, 1996]. Observations from the Mount St. Helens eruption on 18 May 1980 highlight the difference in source conditions between coignimbrite and vent-derived plumes, in particular the occurrence of lofting from the entire extent of the flow resulting in a much larger source radius. While observations of coignimbrite plume formation for much larger events are limited, it is thought that in such cases, lofting also occurs from the entire PDC extent due to buoyancy reversal of the flow [*Sparks et al.*, 1997].

Multiple observations of coignimbrite plume-forming events, in addition to observations from laboratory experiments and outcomes from numerical simulations, highlight the importance of topography, specifically topographic barriers on plume formation [*Andrews and Manga*, 2011, 2012; *Esposti Ongaro et al.*, 2012]. Observations indicate that as the turbulent portion of the flow is forced over a barrier, entrainment and enhanced mixing of ambient air occurs. In addition, the sudden decrease in flow velocity results in mass sedimentation of particles, with both processes resulting in an almost instantaneous decrease in flow density, favoring formation of coignimbrite plumes. Such processes would result in much reduced runout than those predicted here; however, the effect of topography on coignimbrite plume formation is dependent on the relative scale of the current to the topographic barrier [*Andrews and Manga*, 2011, 2012]. Given the type (dilute and turbulent) and scale (initial thickness on the order of hundreds of meters to kilometers) of the flows simulated using the ash flow model, it is likely that topography has a secondary effect on coignimbrite plume formation, but instead, plume formation occurs as the upper portions of the entire flow detach as neutral buoyancy is attained [*Sparks et al.*, 1997] as modeled herein.

Interaction with topographic barriers, causing entrainment of ambient air, also results in a decrease in flow temperature through entrainment of ambient air. However, temperature profiles and variation are difficult to measure during flow propagation or infer from deposits, and therefore, little information regarding flow temperature variation is available in the published record. The results presented here indicate that a greater understanding of flow temperatures, and how it varies spatially, would provide more information regarding the formation of coignimbrite plumes.

The high final flow velocities modeled here agree well with those inferred from the Mount St. Helens' 18 May 1980 coignimbrite-forming event and are interesting with regard to the mechanism of transition from horizontal to vertical momentum. The coupling of the simple one-dimensional models applied here is not capable of accurately describing this transition; however, the results, in addition to the observations from *Eychenne et al.* [2015], imply that the characteristics of flow at liftoff greatly impact the characteristics of the subsequent plume. Outcomes from more complex three-dimensional models, such as PDAC, provide insights into this transition in momentum and how this transition could affect the consequent plume dynamics [*Esposti Ongaro et al.*, 2012].

Two different assumptions have previously been applied in the one-dimensional modeling of coignimbrite plume rise: steady state models assuming a maintained column [*Woods and Wohletz*, 1991; *Calder et al.*, 1997] and a buoyant thermal model [*Woods and Kienle*, 1994] applied to short-lived, discrete clouds. Comparison of both models with observations of coignimbrite plumes formed during the 7 May 1980 Mount St. Helens eruptions indicates that neither type of model completely captures the characteristics of a coignimbrite plume [*Calder et al.*, 1997]. *Woods and Wohletz* [1991] argued that the steady state model is appropriate for the modeling of coignimbrite plumes that form during large volume eruptions whereby a collapsing fountain feeds pyroclastic density currents. The model utilized here makes the same assumptions as those in *Woods and Wohletz* [1991], and for the same entrainment assumption (constant entrainment with height), the trends in radius, velocity, and density (Figure 7) are identical, and similar plume heights are attained for the same initial mass flux [see *Woods and Wohletz*, 1991, Figure 11].

The initial plume vertical velocities calculated from the ash flow model are larger than those previously inferred, although significant challenges likely exist when trying to measure such a characteristic in nature. While large, the values do not seem unreasonable, especially for the scale of events considered here which are larger than those of August 1980 at Mount St. Helens. The inferred vertical velocities pose an interesting question regarding the size of particles lofted into the plume. Comparison of grain size from different events shows that coignimbrite deposits are similar regardless of eruptive conditions. Such deposits are consistently very fine grained [*Engwell and Eychenne*, 2016], with much lower terminal velocities than the range of grain size that could be lofted by the rising mixture at the calculated vertical velocities. To extract only the finest grain sizes into the coignimbrite column, particles within the flow must already be segregated, a phenomenon already well described in the literature [*Valentine*, 1987; *Druitt*, 1998] but also implies that once segregated, particle movement from the dense lower portion into the lofting dilute portion of the flow is difficult, possibly related to different flow regimes of the two flow portions. The plume model results also imply that the initial vertical velocity has a greater control on plume height than previously thought [*Calder et al.*, 1997; *Sparks et al.*, 1997]. Previous studies using one-dimensional models use a considerably lower range in initial vertical velocities, based on a small number of observations from largely channel confined PDCs, and therefore have different characteristics to the events considered here.

Significant differences arise from application of the two different entrainment assumptions. Sensitivity analysis of the plume model has shown that application of a constant radial entrainment coefficient of 0.09 can lead to overestimation of plume heights for large mass flow rates [*Engwell et al.*, 2014]. However, given the complexity of coignimbrite plumes, especially on initiation, it is not clear whether the entrainment assumption utilized here completely captures entrainment in coignimbrite plumes. Such entrainment is likely to only be better understood following observation of further eruptive events and resultant plumes and also by application of numerical models which take into account small-scale processes and formations such as turbulent eddies at the plume edge [*Herzog and Graf*, 2010; *Wang et al.*, 2014; *Cerminara et al.*, 2016].

The plume rise results show that for a given mass flow rate, coignimbrite plumes have similar rise heights and characteristics to Plinian plumes, with neutral buoyancy levels often many kilometers lower than maximum heights. The dominant control on the height of these plumes is the mass flux; however, the choice of entrainment assumption can have significant implications, both for the plume height and plume velocity profiles. Given the fine-grained nature of the ash that is lofted into coignimbrite plumes, and the heights such plumes can attain, such events pose a significant threat to both aviation and downwind infrastructure and populations.

5. Conclusions

Application of the *Bursik and Woods* [1996] ash flow model in combination with formal sensitivity analysis highlights the role of flow temperature and gas mass fraction in the formation of coignimbrite plumes. A number of key observations arise from the model results, relating to the velocity of the final current, and of the coignimbrite plume. Estimates of final flow velocity at coignimbrite formation are in the tens to hundreds of meters per second and are similar to those modeled by *Bursik and Woods* [1996]. Such large velocities support the theory that in the case of large, radial PDC's, coignimbrite plume formation can occur quickly in association with buoyancy reversal of the flow as suggested by *Sparks et al.* [1997] and may not require interaction with topography as is the case for small-scale flows (e.g., Mount Unzen) [*Yamamoto et al.*, 1993]. Furthermore, high final flow velocities describe significant mass flux feeding the coignimbritic plume, shown to be a key

input in controlling plume height. Final flow mass fluxes are used to infer initial plume velocities that in some examples are up to several tens of meters per second. Such high velocities are capable of carrying particles many centimeters in diameter into the atmosphere, yet analysis of coignimbrite plume deposits indicates that they are universally composed of fine-grained ash (<100 μm), indicating that large particles are not available for inclusion into the plume. In combination with the initial radius and liftoff mixture temperature, this initial velocity significantly impacts the final plume height attained. The coupled plume model results correlate first-order initial PDC conditions to the final plume height but are not sufficient for accurately describing the processes that occur during transition from horizontal to vertical momentum and require further investigation using analogue experiments and 2-D/3-D numerical models.

Appendix A: Ash Flow Model Formulation

A modified version of the ash flow model of *Bursik and Woods* [1996] was implemented. The conservation of mass at radius r for a flow thickness $h(r)$, speed $u(r)$, and density $\rho_m(r)$ is calculated as

$$\frac{\mathrm{d}(\rho_m uhr)}{\mathrm{d}r} = \varepsilon \rho_a u r - S, \tag{A1}$$

where ε is the entrainment coefficient and $S = \sum S_i$ is the rate of deposition of pyroclasts of all the sizes.

The propagating current is assumed to have a uniform density with height (i.e., no density stratification):

$$\frac{\mathrm{d}\rho_m u^2 hr}{\mathrm{d}r} = (\rho_m - \rho_a) grh\left(-\frac{\mathrm{d}h}{\mathrm{d}r}\cos\theta + \sin\theta\right) - \frac{1}{2}gh^2 r\cos\theta\frac{\mathrm{d}\rho_m}{\mathrm{d}r} - fu^2 r\rho_m - uS, \tag{A2}$$

whereby the first term on the right-hand side (RHS) represents acceleration associated with changes in flow thickness and gravitational acceleration. In the example here, θ is zero as the runout of the flows is much larger than the scale of topographic variation. The third term represents acceleration variation due to changes in flow density. The forth term represents friction drag, where f is the friction factor dependent on the roughness of the terrain, with an expected range of between 0.001 and 0.02 [*Schlicting*, 1969; *Sparks et al.*, 1978], and the fifth term represents sedimentation. The terms of the momentum equation were reformulated to be a function of the Richardson number, such that

$$\frac{\mathrm{d}u}{\mathrm{d}r}(1 - R_i\cos\theta) = -\frac{u\varepsilon\rho_a}{h\rho_m} + R_i\left(-\frac{(\varepsilon\rho_a u r - S)}{\rho_m hr}\cos\theta + \frac{u}{r}\cos\theta + \frac{u}{h}\sin\theta + \left(-\frac{u}{2(\rho_m - \rho_a)} + \frac{u}{\rho_m}\right)\cos\theta\frac{\mathrm{d}\rho_m}{\mathrm{d}r}\right) - \frac{fu}{h}. \tag{A3}$$

Conservation of total energy, assuming steady flow, is expressed by

$$\frac{\mathrm{d}}{\mathrm{d}r}\left(\rho_m uhr\left(C_m T_m + \frac{p}{\rho_m} + \frac{1}{2}u^2\right)\right) = \varepsilon\rho_a u r\left(C_m T_a + \frac{p}{\rho_a}\right) - SC_s T_m, \tag{A4}$$

where C_m is the mass-averaged specific heat in the flow, C_s is the specific heat of the solid particles, and T_m and T_a are the temperature of the mixture and the ambient, respectively. The unknown flow parameters (u, h, N, and T) are evaluated as a function of distance using equation (A3) and flow bulk density:

$$\rho_m = \left(\frac{nR_m T}{p} + \frac{1-n}{\rho_s}\right)^{-1}, \tag{A5}$$

where n is the average gas content of the flow and ρ_s is the density of the pyroclasts, which in turn require additional transport equations for specific heat of the mixture C_m and gas constant of the mixture R_m to be solved

$$\frac{\mathrm{d}C_m}{\mathrm{d}r} = \frac{C_a - C_m}{\rho_m \epsilon \rho_a u r} + \frac{C_s - C_m}{\rho_a}\left(\frac{-S}{uhr}\right), \tag{A6}$$

$$\frac{\mathrm{d}R_m}{\mathrm{d}r} = \frac{R_a - R_m}{\rho_m nh}\epsilon\rho_a. \tag{A7}$$

Sedimentation of clasts is quantified following *Hazen* [1904], whereby the mass flux M_i of clasts with diameter D_i at a given distance from vent r is related to flow thickness h and velocity u by

$$\frac{\mathrm{d}Mi}{\mathrm{d}r} = -\frac{v_{s,i}M_i}{hu}, \tag{A8}$$

where $v_{s,i}$ is the clast settling velocity, given by equation (1).

Appendix B: Plume Model Formulation

A modified version of the *Bursik* [2001] plume model was applied following *Barsotti et al.* [2008]. Within the model, mass conversation is solved by

$$\frac{\mathrm{d}\left(\rho_m U r^2\right)}{\mathrm{d}s} = 2r\rho_a\left(\alpha \mid U - U_a\cos\varphi \mid + \beta \mid U_a \sin\varphi\right) - 2p\rho_m r(1-n)\sum_{i=1}^{N} v_{s,i}y_i, \tag{B1}$$

where the variation in mass flux (left-hand term) is controlled by air entrainment (RHS first term) and particle loss (RHS second term). The density of ambient air α is a function of atmospheric pressure P, gas constant, and ambient temperature, whereby

$$\alpha = \frac{\mathrm{P}}{R_a T_a}. \tag{B2}$$

The nondimensional variable p describes the probability of each particle falling from the plume as a function of radial entrainment assuming that particles are lost from the sloping margins:

$$p = \frac{\left((1+\frac{6}{5}\alpha)^2 - 1\right)}{\left(1+\frac{6}{5}\alpha\right)^2 + 1} \tag{B3}$$

The variation in solid mass flux is calculated for each particulate phase N:

$$\frac{\mathrm{d}\left(\rho_m U^2(1-n)y_i\right)}{\mathrm{d}s} = -2pv_{s,i}\rho_m r(1-n)y_i \qquad i = 1,\ldots,N. \tag{B4}$$

The momentum balance is solved in both the X and Z components:

$$\frac{\mathrm{d}(\rho_m U r^2(v-U_a))}{\mathrm{d}s} = -r^2\rho_m w\frac{\mathrm{d}U_a}{\mathrm{d}z} - 2pu\rho_m r(1-n)\sum_{i=1}^{N} v_{s,i}y_i, \tag{B5}$$

where the RHS relates to exchange of momentum due to wind (not taken into account here) and momentum loss due to particle loss.

$$\frac{\mathrm{d}(\rho_m U r^2 w)}{\mathrm{d}s} = gr^2(\rho - \rho_m) - 2pw\rho_m r(1-n)\sum_{i=1}^{N} v_{s,i}y_i \tag{B6}$$

where the RHS denotes effect of gravitational acceleration and segregation of particles. The two components of plume velocity along the X and Z axis are v and w, respectively, and are linked by

$$U = \sqrt{v^2 + w^2}. \tag{B7}$$

Conservation of thermal energy is calculated as

$$\frac{\mathrm{d}\left(\rho_m U r^2 C_m T_m\right)}{\mathrm{d}s} = 2r\rho_a C_a T_a\left(\alpha|U - U_a\cos\varphi| + \beta|U_a\sin|\varphi|\right) - r^2 w\rho_a g - T_m P\rho_m r(1-n)\sum_{i=1}^{N} C_{s,i}v_{s,i}y_i, \tag{B8}$$

where the RHS first term describes cooling of the plume by entrainment of ambient air, the second accounts for atmospheric thermal stratification, and the third denotes heat loss due to particle sedimentation.

In the case of the plume model, the bulk density of the mixture is calculated as

$$\rho_m = \left(\frac{n}{\rho_a} + \frac{n-1}{\rho_s}\right)^{-1}. \tag{B9}$$

The specific heat of the mixture is determined by

$$\begin{aligned} C_m = {} & \frac{n\rho_m U r^2(C_{\mathrm{vg}} - C_a)\left(-2\rho_a\left[\alpha(U - U_a\cos\phi) + \beta(U_a\sin\phi)\right] + 2p\rho_m(1-n)\sum_{i=1}^{N} v_{s,i}y_i\right)}{\rho_m^2 U^2 r^3} \\ & + \frac{2\rho_{\mathrm{atm}}\left[\alpha(U - U_a\cos\phi) + \beta(U_a\sin\phi)\right](1-n)\left(C_a - \sum_{i=1}^{N} C_{s,i}y_i\right)}{\rho_m r U} \\ & + \frac{2p(1-n)(nC_a\sum_{i=1}^{N} v_{s,i}y_i + (1-n)\left(\sum_{i=1}^{N} v_{s,i}y_i\sum_{i=1}^{N} C_{s,i} - \sum_{i=1}^{N} v_{s,i}C_{s,i}y_i\right)}{Ur}. \end{aligned} \tag{B10}$$

The transport equation for the gas constant of the mixture is given by

$$\frac{\mathrm{d}R_m}{\mathrm{d}s} = \frac{n_0\rho_{m0}U_0 r_0^2(R_a - R_m)}{n^2\rho_m^2 U^2 r^3} 2\rho_a\left[\alpha|U - U_a\cos\varphi| + \beta|U_a\sin\varphi|\right]. \tag{B11}$$

Notation

ρ	density.
g	gravitational acceleration.
T	temperature.
C	specific heat.
P	pressure.
h	flow thickness.
u	flow velocity.
r	plume or flow radius.
v_s	settling velocity of particles.
S	sedimentation rate within flow.
M_s	solid mass flux of the particles.
Ri	Richardson number.
D_i	particle diameter.
C_d	particle drag coefficient.
f	friction factor dependent on roughness of terrain.
θ	slope angle (herein assumed zero).
ϵ	entrainment coefficient for ash flow.
M	total mass flux of current.
C_v	mass-averaged specific heat of flow.
C_s	specific heat of particles.
n	gas mass fraction.
N	each particulate phase.
C_p	heat capacity.
λ	mass fraction of air entrained in the flow.
z	column height.
α	radial plume entrainment.
β	entrainment due to wind.
U	the velocity of the plume along the center line.
U_ϵ	entrainment velocity.
U_a	the horizontal wind speed.
p	factor representing the probability that a given particle will leave the plume.
s	downstream coordinate for plume model.
y_i	mass fraction of each particle phase.
R_{vg}	gas constant for volcanic gas component.
R_m	gas constant for gas in mixture (comprised both magmatic and ambient).
R_a	gas constant for ambient air.
ϕ	angle between the plume trajectory and ground.
	Subscripts
a	referring to ambient air properties.
vg	referring to volcanic gas properties.
m	referring to mixture properties.
i	referring to particles of a given size fraction.
p	referring to properties of particles.
0	refers to initial condition.

Acknowledgments

S. Engwell was funded by the People Programme (Marie Curie Actions) of the European Union's Seventh Framework Programme (FP7/2007-2013) under the project NEMOH, REA grant agreement 289976. We thank A.B. Clarke and R.S.J. Sparks for their useful discussion. The authors would like to thank Dr. B. Andrews and an anonymous reviewer for their thorough reviews and constructive suggestions that greatly improved the manuscript, and Prof. A. Revil for handling the submission. The models used in this paper will be made available on VHuB and can also be acquired by contacting the corresponding author at samantha@engwell.com.

References

Adams, B. M., L. E. Bauman, W. J. Bohnhoff, K. R. Dalbey, M. S. Ebeida, J. P. Eddy, M. S. Eldred, P. D. Hough, K. T. Hu, J. D. Jakeman, L. P. Swiler, and D. M. Vigil (2009), DAKOTA, A multilevel parallel object-oriented framework for design optimization, parameter estimation, uncertainty quantification, and sensitivity analysis: Version 6.2 user's manual, *Sandia Tech. Rep. SAND2014-4633*, 337, Sandia Natl. Lab., Livermore, Calif., Updated May 2015.

Andrews, B. J. (2014), Dispersal and air entrainment in unconfined dilute pyroclastic density currents, *Bull. Volcanol.*, *76*(9), 1–14, doi:10.1130/G32226.1.

Andrews, B. J., and M. Manga (2011), Effects of topography on pyroclastic density current runout and formation of coignimbrites, *Geology*, *39*(12), 1099–1102, doi:10.1130/G32226.1.

Andrews, B. J., and M. Manga (2012), Experimental study of turbulence, sedimentation, and coignimbrite mass partitioning in dilute pyroclastic density currents, *J. Volcanol. Geotherm. Res.*, *225–226*, 30–44, doi:10.1016/j.jvolgeores.2012.02.011.

Barsotti, S., and A. Neri (2008), The VOL-CALPUFF model for atmospheric ash dispersal: 2. Application to the weak Mount Etna plume of July 2001, *J. Geophys. Res.*, *113*, B03209, doi:10.1029/2006JB004624.

Barsotti, S., A. Neri, and J. S. Scire (2008), The VOL-CALPUFF model for atmospheric ash dispersal: 1. Approach and physical formulation, *J. Geophys. Res.*, *113*, B03208, doi:10.1029/2006JB004623.

Bonadonna, C., et al. (2002), Tephra fallout in the eruption of Soufrière Hills volcano, Montserrat, *Geol. Soc. London Mem.*, *21*(1), 483–516, doi:10.1144/GSL.MEM.2002.021.01.22.

Bursik, M. I. (2001), Effect of wind on the rise height of volcanic plumes, *Geophys. Res. Lett.*, *28*(18), 3621–3624.

Bursik, M. I., and A. W. Woods (1991), Buoyant, superbuoyant and collapsing eruption columns, *J. Volcanol. Geotherm. Res.*, *45*(3–4), 347–350, doi:10.1016/0377-0273(91)90069-C.

Bursik, M. I., and A. W. Woods (1996), The dynamics and thermodynamics of large ash flows, *Bull. Volcanol.*, *58*(2–3), 175–193, doi:10.1007/s004450050134.

Calder, E. S., R. S. J. Sparks, and A. W. Woods (1997), Dynamics of co-ignimbrite plumes generated from pyroclastic flows of Mount St. Helens (7 August 1980), *Bull. Volcanol.*, *58*(6), 432–440, doi:10.1007/s004450050151.

Carazzo, G., and A. M. Jellinek (2012), A new view of the dynamics, stability and longevity of volcanic clouds, *Earth Planet. Sci. Lett.*, *325–326*, 39–51, doi:10.1016/j.epsl.2012.01.025.

Carazzo, G., E. Kaminski, and S. Tait (2008), On the dynamics of volcanic columns: A comparison of field data with a new model of negatively buoyant jets, *J. Volcanol. Geotherm. Res.*, *178*(1), 94–103, doi:10.1016/j.jvolgeores.2008.01.002.

Carey, S. N., and H. Sigurdsson (1988), Experimental studies of particle-laden plumes, *J. Geophys. Res.*, *93*(15), 314–328.

Cerminara, M., T. Esposti Ongaro, and L. C. Berselli (2016), ASHEE-1.0: A compressible, equilibrium-Eulerian model for volcanic ash plumes, *Geosci. Model Dev.*, *9*(2), 697–730.

Cole, P. D., E. S. Calder, T. H. Druitt, R. Hoblitt, R. Robertson, R. S. J. Sparks, and S. R. Young (1998), Pyroclastic flows generated by gravitational instability of the 1996–97 lava dome of Soufrière Hills volcano, Montserrat, *Geophys. Res. Lett.*, *25*(18), 3425–3428.

Costa, A., et al. (2016), Results of the eruption column model intercomparison exercise, *J. Volcanol. Geotherm. Res.*, in press.

de' Michieli Vitturi, M., A. Neri, and S. Barsotti (2015), PLUME-MoM 1.0: A new integral model of volcanic plumes based on the method of moments, *Geosci. Model Dev.*, *8*(8), 2447–2463, doi:10.5194/gmd-8-2447-2015.

de' Michieli Vitturi, M., S. Engwell, S. Barsotti, and A. Neri (2016), Uncertainty quantification and sensitivity analysis of volcanic columns models: Results from the integral model PLUME-MoM, *J. Volcanol. Geotherm. Res.*, doi:10.1016/j.jvolgeores.2016.03.014, in press.

Druitt, T. H. (1998), Pyroclastic density currents, *Geol. Soc. London Spec. Publ.*, *145*(1), 145–182, doi:10.1144/GSL.SP.1996.145.01.08.

Engwell, S. L., and J. Eychenne (2016), Contribution of fine ash to the atmosphere from plumes associated with pyroclastic density currents, in *Volcanic Ash: Hazard Observation*, pp. 67–88, Elsevier.

Engwell, S. L., M. de' Michieli Vitturi, S. Barsotti, and A. Neri (2014), Multiparametric study of wind and atmosphere effect on explosive eruptive style, Abstract V53E-04 presented at 2014 Fall Meeting, AGU, San Francisco, Calif., 15–19 Dec.

Esposti Ongaro, T., A. Neri, G. Menconi, M. de' Michieli Vitturi, P. Marianelli, C. Cavazzoni, G. Erbacci, and P. J. Baxter (2008), Transient 3D numerical simulations of column collapse and pyroclastic density current scenarios at Vesuvius, *J. Volcanol. Geotherm. Res.*, *178*(3), 378–396, doi:10.1016/j.jvolgeores.2008.06.036.

Esposti Ongaro, T., C. Widiwijayanti, A. B. Clarke, B. Voight, and A. Neri (2012), Multiphase-flow numerical modeling of the 18 May 1980 lateral blast at Mount St. Helens, USA, *Geology*, *39*(6), 535–538.

Eychenne, J., J. L. Le Pennec, L. Troncoso, M. Gouhier, and J. M. Nedelec (2012), Causes and consequences of bimodal grain-size distribution of tephra fall deposited during the August 2006 Tungurahua eruption (Ecuador), *Bull. Volcanol.*, *74*(1), 187–205, doi:10.1007/s00445-011-0517-5.

Eychenne, J., K. Cashman, A. Rust, and A. Durant (2015), Impact of the lateral blast on the spatial pattern and grain size characteristics of the 18 May 1980 Mount St. Helens fallout deposit, *J. Geophys. Res. Solid Earth*, *120*, 6018–6038, doi:10.1002/2015JB012116.

Hazen, A. (1904), On sedimentation, *Trans. Am. Soc. Civ. Eng.*, *53*(2), 45–71.

Herzog, M., and H. F. Graf (2010), Applying the three-dimensional model ATHAM to volcanic plumes: Dynamic of large co-ignimbrite eruptions and associated injection heights for volcanic gases, *Geophys. Res. Lett.*, *37*, L19807, doi:10.1029/2010GL044986.

Holasek, R. E., S. Self, and A. W. Woods (1996), Satellite observations and interpretation of the 1991 Mount Pinatubo eruption plumes, *J. Geophys. Res.*, *101*(B12), 27,635–27,655, doi:10.1029/96JB01179.

Horwell, C. J., L. P. Brana, R. S. J. Sparks, M. D. Murphy, and V. L. Hards (2001), A geochemical investigation of fragmentation and physical fractionation in pyroclastic flows from the Soufrière hills volcano, Montserrat, *J. Volcanol. Geotherm. Res.*, *109*, 247–262.

Huppert, H., J. S. Turner, S. N. Carey, R. S. J. Sparks, and M. A. Hallworth (1986), A laboratory simulation of pyroclastic flows down slopes, *J. Volcanol. Geotherm. Res.*, *30*, 179–199.

Levine, A. H., and S. W. Kieffer (1991), Hydraulics of the August 7, 1980, pyroclastic flow at Mount St. Helens, Washington, *Geology*, *19*, 1121–1124, doi:10.1130/0091-7613(1991)019<1121.

Miyabuchi, Y. (1999), Deposits associated with the 1990–1995 eruption of Unzen volcano, Japan, *J. Volcanol. Geotherm. Res.*, *89*(1–4), 139–158, doi:10.1016/S0377-0273(98)00129-2.

Morton, B. R., G. Taylor, and J. S. Turner (1956), Turbulent gravitational convection from maintained and instantaneous sources, *Proc. R. Soc. A*, *234*(1196), 1–23, doi:10.1098/rspa.1956.0011.

Neri, A., and F. Dobran (1994), Influence of eruption parameters on the thermofluid dynamics of collapsing volcanic columns, *J. Geophys. Res.*, *99*, 11,833–11,857, doi:10.1029/94JB00471.

Neri, A., A. Di Muro, and M. Rosi (2002), Mass partition during collapsing and transitional columns by using numerical simulations, *J. Volcanol. Geotherm. Res.*, *115*(1), 1–18.

Neri, A., T. Esposti Ongaro, G. Macedonio, and D. Gidaspow (2003), Multiparticle simulation of collapsing volcanic columns and pyroclastic flow, *J. Geophys. Res.*, *108*(B4), 2202, doi:10.1029/2001JB000508.

Parker, G., M. Garcia, Y. Fukushima, and W. Yu (1987), Experiments on turbidity currents over an erodible bed, *J. Hydraul. Res.*, *25*(1), 123–147.

Saltelli, A., M. Ratto, T. Andres, F. Campolongo, J. Cariboni, D. Gatelli, M. Saisana, and S. Tarantola (2008), *Global Sensitivity Analysis: The Primer*, John Wiley, Chichester, England.

Schlicting, H. (1969), *Boundary Layer Theory*, McGraw Hill, New York.

Sparks, R. S. J., L. Wilson, and G. Hulme (1978), Theoretical modeling of the generation, movement, and emplacement of pyroclastic flows by column collapse, *J. Geophys. Res.*, *83*(B4), 1727, doi:10.1029/JB083iB04p01727.

Sparks, R. S. J., J. G. Moore, and C. J. Rice (1986), The inital giant umbrella cloud of the May 18th 1980 explosive eruption of Mount St. Helens, *J. Volcanol. Geotherm. Res.*, *28*, 257–274.

Sparks, R. S. J., R. T. Bonnecaze, H. E. Huppert, J. R. Lister, M. A. Hallworth, H. Mader, and J. Phillips (1993), Sediment-laden gravity currents with reversing buoyancy, *Earth Planet. Sci. Lett.*, *114*, 243–257, doi:10.1016/0012-821X(93)90028-8.

Sparks, R. S. J., M. I. Bursik, S. N. Carey, J. Gilbert, L. S. Glaze, H. Sigurdsson, and A. W. Woods (1997), *Volcanic Plumes*, Wiley, New York.

Valentine, G. A. (1987), Stratified flow in pyroclastic surges, *Bull. Volcanol.*, *49*(4), 616–630, doi:10.1007/BF01079967.

Yamamoto, T., S. Takarada, and S. Suto (1993), Pyroclastic flows from the 1991 eruption of Unzen volcano, Japan, *Bull. Volcanol.*, *55*(3), 166–175.

Wang, R. Q., A. Wing-Keung Law, and E. E. Adams (2014), Large-eddy simulation (LES) of settling particle cloud dynamics, *Int. J. Multiphase Flow*, *67*, 65–75, doi:10.1016/j.ijmultiphaseflow.2014.08.004.

Watanabe, K., K. Ono, K. Sakaguchi, A. Takada, and H. Hoshizumi (1999), Co-ignimbrite ash-fall deposits of the 1991 eruptions of Fugen-dake, Unzen volcano, Japan, *J. Volcanol. Geotherm. Res.*, *89*(1–4), 95–112, doi:10.1016/S0377-0273(98)00126-7.

Woods, A. W. (1988), The fluid dynamics and thermodynamics of eruption columns, *Bull. Volcanol.*, *50*(3), 169–193.

Woods, A. W., and P. C. Caulfield (1992), A laboratory study of explosive volcanic eruptions, *J. Geophys. Res.*, *97*(B5), 6699–6712.

Woods, A. W., and J. Kienle (1994), The dynamics and thermodynamics of volcanic clouds: Theory and observations from the April 15 and April 21, 1990 eruptions of Redoubt Volcano, Alaska, *J. Volcanol. Geotherm. Res.*, *62*, 273–299.

Woods, A. W., and K. H. Wohletz (1991), Dimensions and dynamics of co-ignimbrite eruption columns, *Nature*, *350*, 225–227.